Chaos, Solitons and Fractals 164 (2022) 112718

Contents lists available at ScienceDirect

Chaos, Solitons and Fractals

journal homepage: www.elsevier.com/locate/chaos

Chaotic pitch motion of an aerodynamically stabilized magnetic satellite in polar orbits

Vladimir S. Aslanov [a,*], Dmitry A. Sizov [a,b]

[a] Samara National Research University, 34, Moscovskoe shosse, Samara 443086, Russia
[b] Syzran Branch of Samara State Technical University, 45, Sovetskaya St., Syzran 446001, Russia

ARTICLE INFO

Keywords:
CubeSats
LEO
Aerodynamic stabilization
Magnetic torque
Chaotic attitude dynamics
Melnikov method

ABSTRACT

The paper is devoted to the chaotic attitude dynamics of magnetic satellites with stabilizing panels. The pitch motion under the gravitational and restoring aerodynamic torques and small perturbations, namely, the magnetic torque and the aerodynamic damping, is considered. On the example of a CubeSat having an aerodynamic instability, it is demonstrated that the unperturbed phase space evolves with orbital altitude both quantitatively and qualitatively, forming different sets of homoclinic and heteroclinic trajectories. The Melnikov method is used to find the combinations of system parameters resulting in regular and chaotic motions. The occurrence of chaos is verified by means of Poincaré sections.

1. Introduction

The field of the chaotic motion of satellites, in particular, chaos in orbital parameters evolution [1–8], and chaotic attitude motion [9–22] has received considerable attention in recent years. The features of attitude motion depend largely on the type of satellite, and thus there are many specific works in the literature addressing the chaotic attitude motion of dumbbell satellites [16,19], gyrostats [15,17,18,20,23], or CubeSats [21,22]. If a satellite is in LEO or very low Earth orbit (VLEO, typically characterized by altitudes of 80–450 km), its interaction with the atmosphere needs to be taken into account. The restoring aerodynamic torque resulting from this interaction can be used for angular stabilization. The passive aerodynamic stabilization is the simplest, since it does not require any power supply. This type of stabilization has been studied since the late 50s [24–27], but previously it was mainly used for large satellites. Currently, with the growing popularity of micro-, nano-, and picosatellites, which are more sensitive to the interaction with the air, the number of missions using partial or total aerodynamic stabilization has increased substantially. For example, this type of stabilization is realized for the QARMAN CubeSat [28], launched in 2020, and the SOAR nanosatellite [29], launched in 2021, meant to investigate the atmospheric flow regime in VLEO. Aerodynamic stabilization on CubeSats is commonly realized by means of flat tail panels [21,22,28–34].

It is usually assumed that, during its mission, the satellite will be in the vicinity of a stable equilibrium position, characterized by a zero angle of attack. However, for certain aerodynamic layouts, intermediate trim positions, characterized by non-zero angle of attack, may exist. The satellite may get to one of these positions because of an accidental disturbance, which may happen, for example, when the satellite separates from the launch vehicle, or if the tail panels are deployed inaccurately. Complete elimination of these positions is not always possible, therefore, in the authors' opinion, more research is needed in the field of attitude motion in the vicinity of these positions, especially considering the possibility of chaos that can be caused by disturbances of different nature, such as variable inertia matrix [9], orbit eccentricity [9,13], elastic elements [11,12,21,22], magnetic torque [13,14]. Another important aspect is the influence of the damping aerodynamic torque [35]. It is often neglected, since its magnitude is usually much lower than the magnitude of the aerodynamic restoring torque. But in the presence of the unstable equilibrium positions and the above-mentioned disturbances, the damping aerodynamic torque may substantially affect the character of the attitude motion, especially in VLEO.

The goal of the paper is to investigate chaos in the attitude motion of satellites in low orbits under the action of aerodynamic, gravitational, and magnetic torques and to find combinations of system parameters corresponding to chaotic and regular motions. In order to achieve the goal, the unperturbed and perturbed motions of an aerodynamically stabilized magnetic satellite are defined, the equilibrium positions are studied, the altitude evolution of the unperturbed phase space is discussed. To detect chaos in the perturbed motion, the Melnikov method is used. Verification of the discovered effects is performed by means of

* Corresponding author.
E-mail addresses: aslanov_vs@mail.ru (V.S. Aslanov), sizov.syzran@gmail.com (D.A. Sizov).
URL: https://aslanov.ssau.ru (V.S. Aslanov).

https://doi.org/10.1016/j.chaos.2022.112718
Received 29 June 2022; Received in revised form 16 August 2022; Accepted 18 September 2022

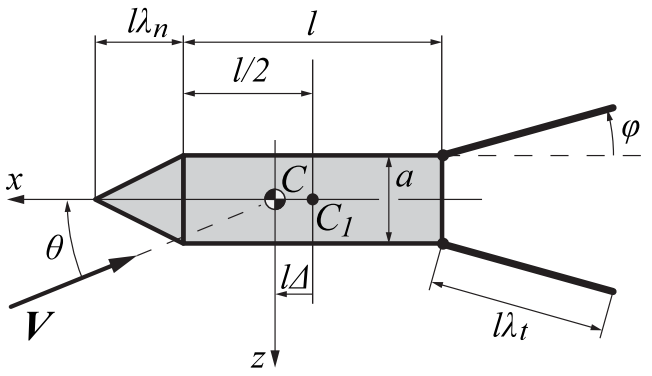

Fig. 1. Satellite with stabilizing side panels. For clarity, only two of four panels are depicted.

the Poincaré sections. As a result, a procedure for obtaining the regions in the system parameters space providing regular and chaotic attitude motions was introduced, which constitutes the novelty of this study.

The paper is organized as follows. In Section 2, the problem is formulated and the equations of the perturbed and unperturbed motion are presented, the latter taking into account the restoring and damping aerodynamic torques as well as the gravitational and magnetic torques. Section 3 discusses the evolution of the unperturbed phase space for a particular aerodynamically stabilized magnetic satellite. In Section 4, the Melnikov method is used to find the conditions of existence of chaos. Section 5 illustrates different cases of chaotic and regular motion via Poincaré surfaces. Finally, conclusions are given in Section 6.

2. Problem statement. Equations of perturbed and unperturbed motion

Consider a magnetic satellite with additional aerodynamic surfaces (Fig. 1). Let us make several assumptions regarding the attitude motion of the satellite.

1. The satellite is in the circular polar orbit.
2. The magnetic moment of the satellite is constant and aligned with the principal axis z of the satellite (Fig. 1).
3. The roll and yaw motions are initially quiescent.

It can be shown [13] that, in the case defined by the above assumptions, the roll and yaw motions are not excited by the pitch motion, and the direction of the principal axis y of the satellite remains normal to its orbital plane. In this case, the orientation of the satellite can be described by the pitch angle θ between the local horizontal and longitudinal axis x of the satellite. As the goal of the paper is to demonstrate chaos in the attitude motion under the combined action of the gravitational, aerodynamic, and magnetic torques, it is enough to take the simplest case of rotation in the orbital plane, since the presence of chaos in this particular case means that it is actually present in the general case. Moreover, it is in the planar case that the largest amplitudes of the angle of attack are observed, since all the potential energy of attitude motion stored in the satellite is transformed into the kinetic energy of rotation around only one axis. Thus, this type of chaotic motion is the most concerning in practice and, therefore, it needs to be investigated in detail.

With all the above assumptions taken into account, let us write the equation of the pitch motion of the satellite:

$$J_y\ddot{\theta} = M_g + M_m + M_a \tag{1}$$

where J_y is the transverse moment of inertia about the principal axis y, M_g, M_m, M_a are the gravitational, magnetic, and aerodynamic torques, respectively. The well-known expression for the gravitational torque in the orbital plane is

$$M_g = \frac{3}{2}n^2\left(J_z - J_x\right)\sin 2\theta \tag{2}$$

where J_z and J_x are the transverse and longitudinal moments of inertia, respectively, n is the mean motion,

$$n = \sqrt{\frac{\mu}{R_0^3}}, \tag{3}$$

μ is the gravitational parameter of the Earth, $R_0 = R + h$ is the orbit radius, R is the mean radius of the Earth, h is the orbital altitude. The magnetic torque acting in the orbital plane can be expressed as [36,37]

$$M_m = \frac{M\mu_0\mu_m}{4\pi R_0^3}\left(\cos\theta\cos\nu - 2\sin\theta\sin\nu\right) \tag{4}$$

where $\mu_0 = 1.256\cdot 10^{-6}$ N A^{-2} is the magnetic permeability of free space, $\mu_m \approx 7.7\cdot 10^{22}$ A m^2 is the geomagnetic dipole moment, M is the magnitude of the vector of the own magnetic moment of the satellite. The aerodynamic torque M_a can be written as a sum of two components:

$$M_a(h,\theta,\dot{\theta}) = M_r(h,\theta) + M_d(h,\theta,\dot{\theta}) \tag{5}$$

where M_r is the restoring torque,

$$M_r(h,\theta) = C_m(\theta)\frac{\rho(h)V(h)^2}{2}lA, \tag{6}$$

and M_d is the damping torque proportional to the angular speed:

$$M_d(h,\theta,\dot{\theta}) = C_m^{\dot{\theta}}(\theta)\frac{\rho(h)V(h)}{2}l^2A\dot{\theta}. \tag{7}$$

In Eqs. (6) and (7), A is the reference area taken equal to the satellite body cross-section area, l is the reference length taken equal to the satellite body length, $V = \sqrt{\mu/R_0}$ is the orbital velocity, ρ is the air density, C_m and $C_m^{\dot{\theta}}$ are the restoring and damping aerodynamic torque coefficients, respectively. For the convenience of analysis, these coefficients can be represented by Fourier series:

$$C_m(\theta) = \sum_{j=1}^{k} b_{\theta j}\sin j\theta, \tag{8}$$

$$C_m^{\dot{\theta}}(\theta) = \frac{a_{\dot{\theta}_0}}{2} + \sum_{j=1}^{k} a_{\dot{\theta}j}\cos j\theta \tag{9}$$

where k is the number of harmonics. Taking into account Eqs. (5)–(7) and using the true anomaly $\nu = nt$ as a dimensionless time, one can rewrite Eq. (1) to obtain the equation of perturbed motion in dimensionless form as follows:

$$\theta'' - \alpha(h)C_m(\theta) - \beta\sin 2\theta = \gamma(\cos\theta\cos\nu - 2\sin\theta\sin\nu) + \delta(h)C_m^{\dot{\theta}}(\theta)\theta' \tag{10}$$

where $(\quad)'$ means differentiation with respect to the true anomaly,

$$\alpha = \frac{Al(h+R)^2\rho(h)}{2J_y}, \tag{11}$$

$$\beta = \frac{3\left(J_z - J_x\right)}{2J_y}, \tag{12}$$

$$\gamma = \frac{M\mu_0\mu_m}{4\pi\mu J_y}, \tag{13}$$

$$\delta = \frac{Al^2\left(h+R\right)\rho(h)}{2J_y} \tag{14}$$

are dimensionless coefficients. Note that the right-hand side of Eq. (10) contains only small terms. The first of them is the periodic perturbation due to the magnetic torque. The second term is the damping caused by the interaction with the air.

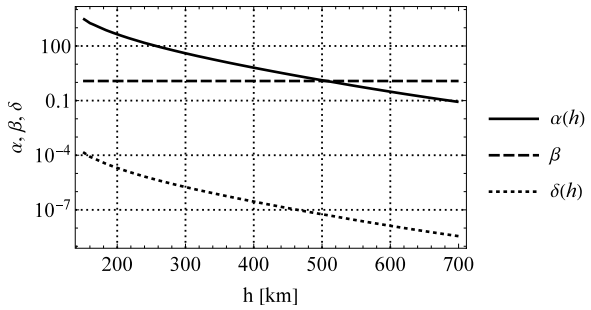

Fig. 2. Non-dimensional coefficients of the equation of perturbed motion Eq. (10).

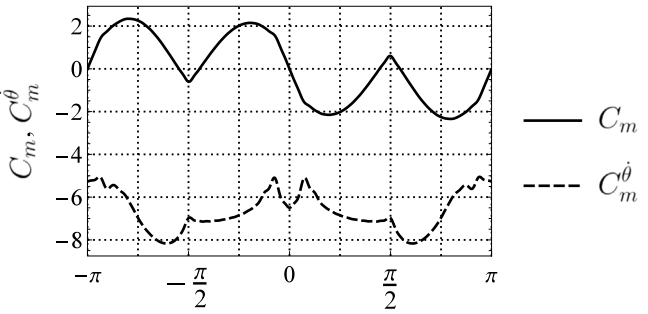

Fig. 3. Coefficients of restoring and damping aerodynamic torques for the example satellite.

The equation of unperturbed motion can be obtained by omitting the above-mentioned small terms in the right-hand side of Eq. (10) and contains only restoring aerodynamic and gravitational torques:

$$\theta'' - \alpha(h) C_m(\theta) - \beta \sin 2\theta = 0. \tag{15}$$

Taking into account Eq. (8), Eq. (15) can be rewritten in order to obtain the equation of the unperturbed motion in its final form:

$$\theta'' = \alpha(h) \sum_{j=1}^{k} b_{\theta j} \sin j\theta + \beta \sin 2\theta. \tag{16}$$

Note that due to the presence of many harmonics in the Fourier series needed to express the restoring aerodynamic torque coefficient, the unperturbed phase space is significantly more complex than in the case of action of the gravitational torque alone. The Eq. (16) has an energy integral

$$E = \frac{1}{2}\theta'^2 + U(\theta, h) = const \tag{17}$$

where U is the potential function,

$$U(\theta, h) = \alpha(h) \sum_{j=1}^{k} \frac{b_{\theta j}}{j} \cos j\theta + \frac{1}{2}\beta \cos 2\theta. \tag{18}$$

The shape of the potential function and hence the structure of the unperturbed phase space significantly depend on the orbital altitude h. This dependence will be discussed in detail in the next section.

3. Evolution of heteroclinic and homoclinic orbits with orbital altitude

In this section, the evolution of the unperturbed phase space for a particular satellite is discussed. In order to obtain its equilibrium positions and the separatrices of the phase space for different orbital altitudes, the coefficients of the equation of the perturbed motion, the dimensionless torques acting on the satellite, and the corresponding potential energy are analyzed.

The structure of the phase space corresponding to the equation of unperturbed motion Eq. (16) is determined by the coefficients α, β, and $b_{\theta j}$. The ratio of the first two coefficients, in its turn, largely depends on the orbital altitude h, as it can be seen from Fig. 2. Indeed, the coefficient α (Eq. (11)) changes by several orders of magnitude in the altitude interval from 150 to 700 km, mostly due to the change in air density. On the contrary, the second coefficient determining the unperturbed motion, β, is associated with the gravitational torque and, by virtue of Eq. (12), does not depend on altitude. Fig. 2 also shows the evolution of the coefficient δ (Eq. (14)), which determines the degree of aerodynamic damping. It can be seen that this coefficient remains several orders of magnitude smaller than α and β, so the choice of undisturbed motion is justified.

The coefficients $b_{\theta j}$ determine the shape of the restoring aerodynamic torque curve and change very slightly with altitude, so given the significant change in α, they can be considered constant. These coefficients are determined by the geometric parameters of the satellite, so it is difficult to analyze the unperturbed motion without choosing a particular shape of the satellite. In this paper, we consider a CubeSat with pyramidal nose and tail panels [22,33] (Fig. 1) to which we will refer as the example satellite. Its configuration is typical for LEO and VLEO satellites [28–32,34] and it is characterized by several parameters collected in Table 1. The most important of them are the satellite body length l, panels deployment angle φ, the dimensionless nose and tail panels lengths λ_n and λ_t, respectively, dimensionless longitudinal shift Δ of the center of mass of the satellite C from the geometric center C_1 of its body. The parameter Δ is considered positive if the center of mass is shifted closer to the nose of the satellite. The aerodynamic characteristics of the example satellite are shown in Fig. 3. They were calculated using the Schaaf and Chambre's approach [38], taking into account that at the CubeSats operational altitudes (above 120 km) the Knudsen number Kn is larger then 10, which means that the flow is free molecular [39]. The assumptions related to the calculation of the aerodynamic characteristics of the satellite were the following:

1. The reflected air molecules speed distribution is Maxwellian.
2. The center of mass of the satellite lies on its longitudinal axis.
3. Additional aerodynamic surfaces are modeled as rigid thin flat plates.
4. The density and temperature of the incident stream at different altitudes are chosen using Jacchia–Bowman 2008 Atmosphere Model [40] assuming mean solar activity.

The calculated curves $C_m(\theta)$ and $C_m^{\dot\theta}(\theta)$ for the example satellite (Fig. 3) are kinked due to the existence of the angular positions where the shielding of some elements of the satellite begins or ends. In order to accurately describe the complex shape of these curves, it is necessary to use a significant number of harmonics k in the Fourier series represented by Eqs. (8) and (9). In this paper, we take $k = 50$. The amplitudes for all harmonics are given in Appendix.

It should be noted that the curve of the restoring torque coefficient $C_m(\theta)$ has zeros in the vicinity of points $\theta = \pm\pi/2$, which indicates that the satellite has intermediate equilibrium positions. This aerodynamic instability significantly complicates the structure of the unperturbed phase portrait, which will be discussed below.

The unperturbed motion evolution with orbital altitude is shown in Fig. 4. In order to illustrate qualitative changes in phase space for the example satellite, it is sufficient to take three different orbital altitudes. Here we choose the altitudes of 500, 575, and 650 km. Fig. 4 depicts the dimensionless torque $-\partial U/\partial\theta$ proportional to the sum of the gravitational torque M_g (Eq. (2)) and restoring aerodynamic torque M_r (Eq. (6)), the potential function U (Eq. (18)), and the separatrices of the phase space corresponding to this function. Let us first consider the dimensionless torque curves (Fig. 4, top). The presence of distinctive kinks in the graphs a and b indicates that the aerodynamic torque dominates at an altitude of 500 km and maintains its effect on the

Table 1
Parameters of the example satellite.

Parameter	Value
Number of standard CubeSat units u	3
Satellite body length l	0.3 m
Satellite body width a	0.1 m
Reference area A	0.01 m^2
Longitudinal moment of inertia J_x	0.0088 kg m^2
Transverse moment of inertia $J_y = J_z$	0.043 kg m^2
Relative longitudinal shift of satellite CoM Δ	−0.262
Nose relative length λ_n	1/3
Tail panels relative length λ_t	2/3
Tail panels deployment angle φ	30°

pitch motion at an altitude of 575 km as well. However, with a further increase in altitude, according to Fig. 2, the coefficient α decreases so much that the gravitational torque begins to dominate, which can be clearly seen in the $-\partial U/\partial\theta$ curve for 650 km, which is free of kinks. The points of intersection of the $-\partial U/\partial\theta$ curves with the abscissa axis correspond to the equilibrium positions of the satellite. Fig. 5 represents the evolution of these positions in the orbital altitude range from 150 to 700 km. These positions are of different types, as it can be clearly seen in the curves of the potential function U (Fig. 4, middle). The stable equilibrium positions (centers) $\theta_{c0} = 0$, θ_{c1}, θ_{c2} correspond to the local minima of the potential function, and unstable equilibrium positions (saddle points) $\theta_{s0} = 0$, $\theta_{s1} = -\pi$, θ_{s2}, $\theta_{s3} = -\theta_{s2}$, $\theta_{s4} = \pi$ correspond to the local maxima. The positions $\theta_{s3} = -\theta_{s2}$, whose existence is mainly caused by the above-mentioned aerodynamic instability, are of particular interest, because they are forming an additional separatrix of the phase space, to which we will refer as the inner separatrix. Another well-known separatrix corresponding to the positions $\theta_{s1} = -\pi$ and $\theta_{s4} = \pi$ is always present when the planar unperturbed motion is influenced by the aerodynamic torque, and it can be called the outer separatrix. Fig. 4, bottom depicts the phase portrait of the unperturbed system and the two above-mentioned separatrices. The unstable equilibria $\theta_{s1} = -\pi$ and $\theta_{s4} = \pi$ corresponding to the outer separatrix are connected by four heteroclinic orbits. The unstable equilibria θ_{s2} and $\theta_{s3} = -\theta_{s2}$ corresponding to the inner separatrix are also connected by the other four heteroclinic orbits. Note that, on the inner separatrix, there also exist four homoclinic trajectories with the same energy as the heteroclinic ones. Two of them correspond to the saddle point θ_{s2} and the other two to the saddle θ_{s3}.

It is worth noting that the inner heteroclinic orbits exist only up to the critical altitude h_*, which is the root of the equation

$$\left.\frac{\partial^2 U(\theta,h)}{\partial\theta^2}\right|_{\theta=0} = 0. \tag{19}$$

For the example satellite, $h_* = 600021$ m. It can be seen that at an altitude of 650 km (Fig. 4, *c*, bottom), which is larger than the critical one, the inner heteroclinic orbits no longer exist. Thus, changing in altitude alters the unperturbed phase portrait not only quantitatively, but also qualitatively. Equations for all above-mentioned separatrices can be obtained by solving the differential equation

$$\theta'^{\pm}(h,\nu) = \omega^{\pm}(h,\nu) = \pm\sqrt{2}\sqrt{U(h,\theta_{s_i}) - U(h,\theta(\nu))}; \quad i = 0,1,2. \tag{20}$$

For the outer separatrix $i = 1$, for the inner separatrix $i = 2$, $h \le h_*$; $i = 0$, $h > h_*$. Due to the complexity of the potential function U (Eq. (18)), which, for the example satellite, is represented by a sum of more than 50 terms, Eq. (20) can be solved only numerically. The resulting equations for homoclinic and heteroclinic orbits $\boldsymbol{z}^{\pm} = \left(\theta^{\pm}(h,\nu), \omega^{\pm}(h,\nu)\right)$ will be used in the following section for detection of chaos.

4. Melnikov method

This section is devoted to the investigation of the perturbed system. In this case, the pitch motion of the satellite near the unperturbed separatrices becomes extremely complicated, a stochastic layer appears near these separatrices, and the stable and unstable manifolds may intersect. Here we will use the Melnikov method [41–43], on the one hand, to demonstrate the possibility of homoclinic and heteroclinic intersections, and, on the other hand, to find the conditions of existence of chaos determined by the coefficient of the magnetic perturbation γ, which depends on the own magnetic moment of the satellite and can be chosen arbitrarily, and the orbital altitude h.

4.1. Melnikov functions

In order to apply the Melnikov method [41–43], the nonautonomous equation of the second order Eq. (16) can be expressed as the following system of two autonomous equations of the first order:

$$\begin{aligned} &\theta' = \omega = f_1 + g_1, \\ &\omega' = \alpha(h)C_m(\theta) + \beta\sin 2\theta \\ &\quad +\gamma(\cos\theta\cos\nu - 2\sin\theta\sin\nu) + \delta(h)C_m^{\dot\theta}(\theta)\omega = f_2 + g_2 \end{aligned} \tag{21}$$

where $f_1 = \omega$, $g_1 = 0$, $f_2 = \alpha(h)C_m(\theta) + \beta\sin 2\theta$, and $g_2 = \gamma(\cos\theta\cos\nu - 2\sin\theta\sin\nu) + \delta(h)C_m^{\dot\theta}(\theta)\omega$. The Melnikov function $M^{\pm}(h,\nu_0)$ for the system Eq. (21) is given by

$$\begin{aligned} M^{\pm}(h,\gamma,\nu_0) &= \int_{-\infty}^{\infty} f_1\left[\boldsymbol{z}^{\pm}(\nu)\right] g_2\left[\boldsymbol{z}^{\pm}(\nu), \nu+\nu_0\right] d\nu \\ &= \int_{-\infty}^{\infty} \omega^{\pm}(\nu)\{\gamma(\cos\theta^{\pm}(h,\nu)\cos(\nu+\nu_0) - 2\sin\theta^{\pm}(h,\nu) \\ &\quad \times\sin(\nu+\nu_0)) + \delta(h)C_m^{\dot\theta}(\theta^{\pm}(h,\nu))\omega^{\pm}(h,\nu)\}d\nu \\ &= \gamma\int_{-\infty}^{\infty}\omega^{\pm}(h,\nu)\left(\cos\theta^{\pm}(h,\nu)\cos(\nu+\nu_0)\right. \\ &\quad \left.-2\sin\theta^{\pm}(h,\nu)\sin(\nu+\nu_0)\right)d\nu \\ &\quad +\delta(h)\int_{-\infty}^{\infty}\left(\omega^{\pm}(h,\nu)\right)^2 C_m^{\dot\theta}(\theta^{\pm}(h,\nu))d\nu = M_\gamma(\nu_0) + M_\delta \end{aligned} \tag{22}$$

where $\boldsymbol{z}^{\pm} = \left(\theta^{\pm}(\nu), \omega^{\pm}(\nu)\right)$ are the solutions of Eq. (20) giving the unperturbed orbits, $M_\gamma(\nu_0)$ is a periodic term representing the degree of disturbance, M_δ is a constant term giving the degree of damping. It is worth noting that, in the problem under consideration, due to the complexity of the integrals in Eq. (22), the Melnikov functions are calculated numerically, separately for all three different sets of unperturbed homoclinic and heteroclinic orbits described in the previous section. If the Melnikov function has simple zeros, then there exist transverse intersections between the stable and unstable manifolds of hyperbolic trajectories [44]. In our problem, it means chaos in the pitch motion.

4.2. Regions of explicit regular and chaotic motions

For the aerodynamically stabilized magnetic satellite, it is mandatory to predict the combinations of system parameters for which the aerodynamic damping is no longer able to compensate the perturbations caused by the magnetic torque. For practical purposes, it is particularly important to find the boundaries of the chaotic regions as a set of combinations of parameters h and γ, such that there exist second-order zeros ν_0^* for which

$$\begin{cases} M^{\pm}(h,\gamma,\nu_0^*) = 0, \\ \dfrac{d}{d\nu}M^{\pm}(h,\gamma,\nu_0)\Big|_{\nu_0=\nu_0^*} = 0. \end{cases} \tag{23}$$

Clearly, these equations describe the case when the curve $M^{\pm}(h,\gamma,\nu_0)$ touches the axis of abscissa. Fig. 6, *a, b, c* shows the boundaries of the chaotic regions for the example satellite corresponding to the inner heteroclinic orbits, to the inner homoclinic orbits, and to the outer heteroclinic orbits, respectively, calculated using Eq. (23). To illustrate the dependence of the Melnikov function on the coefficient γ, several points are chosen in the vicinity of each boundary: I_1, I_2, I_3 for the inner heteroclinic orbits, I_3, I_4, I_5 for the outer heteroclinic orbits, O_1, O_2, O_3 for the outer heteroclinic orbits. Fig. 7 depicts the Melnikov

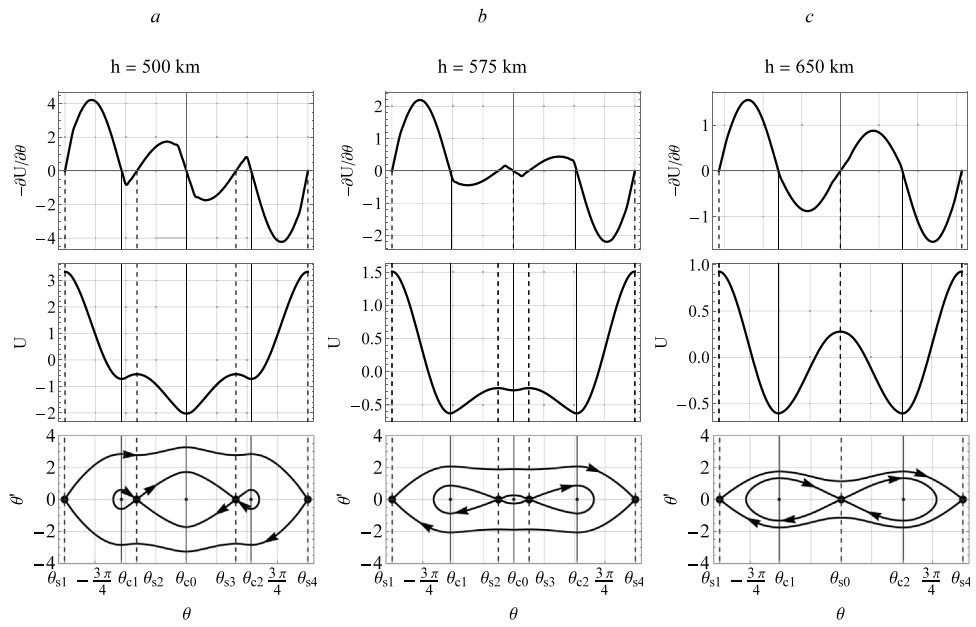

Fig. 4. Torques, potential function, and separatrices corresponding to the unperturbed motion of the example satellite.

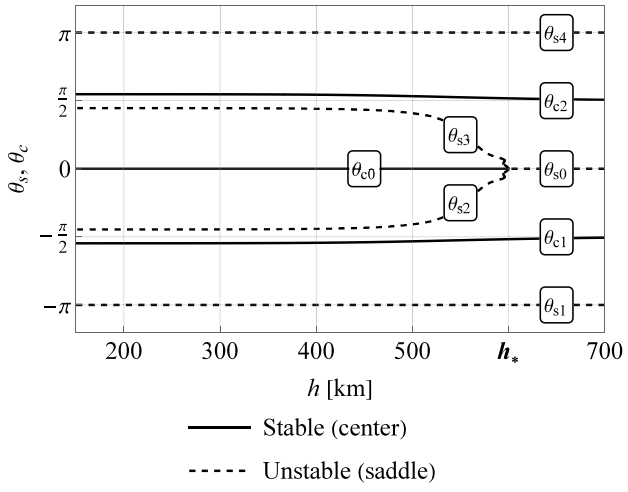

Fig. 5. Equilibrium positions of the example satellite.

functions for these points. It can be seen that the Melnikov functions for the points I_2, I_5, and O_2, lying on the calculated boundaries of the chaotic regions, touch the abscissa axis and thus satisfy the condition represented by Eq. (23).

Of particular importance for practice is Fig. 6, *d*, depicting the resultant boundary of the chaotic region (bold black dashed line) and the boundary of regular motion (bold black solid line), which were obtained by combining the three above-mentioned boundaries corresponding to three different sets of unperturbed orbits. From Fig. 6, *d*, it can be clearly seen that, for a given altitude h, any value of the coefficient γ such that the point (h, γ) lies in the gray area below the chaotic boundary ensures regular pitch motion. This region can be characterized as "weak magnetic perturbation, strong aerodynamic damping". Fig. 8 represents the Melnikov functions corresponding to all three sets of unperturbed orbits for an arbitrarily chosen example point A lying in this region. It can be seen that, as expected, none of these functions has simple zeros. The region of chaotic motion (orange area in Fig. 6, *d*) can be characterized as "strong magnetic perturbation, weak aerodynamic damping". For all combinations of the coefficient γ

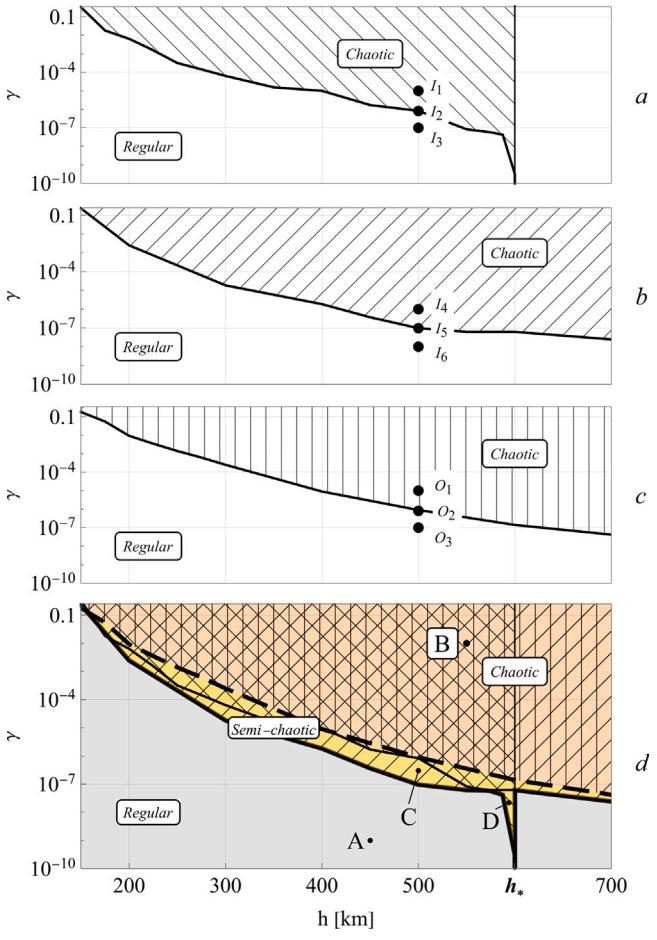

Fig. 6. Regions of regular and chaotic pitch motions for the example satellite: *a*—for inner heteroclinic orbits; *b*—for inner homoclinic orbits; *c*—for outer orbits; *d*—combined plot for all three sets of unperturbed orbits.

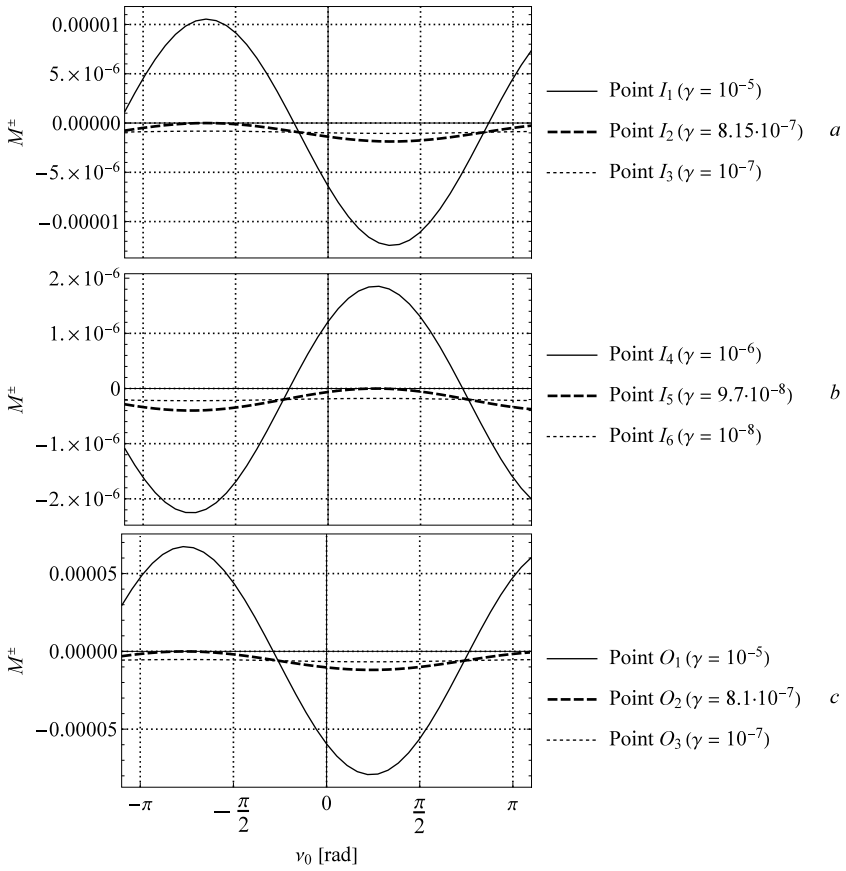

Fig. 7. Melnikov functions for the example satellite (h = 500 km): *a*—for inner heteroclinic orbits; *b*—for inner homoclinic orbits; *c*—for outer orbits.

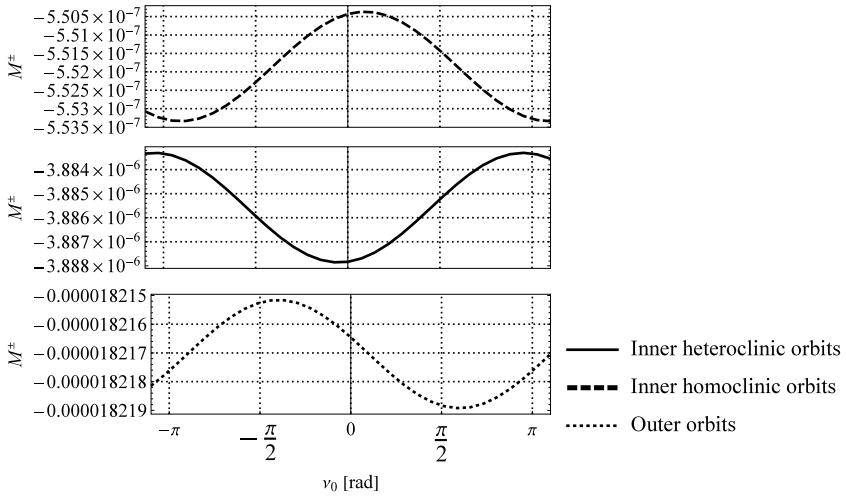

Fig. 8. Melnikov functions corresponding to point A (h = 450 km, $\gamma = 10^{-9}$) in Fig. 6, *d*.

and orbital altitude in this region, the pitch motion of the satellite will be chaotic. The Melnikov functions for an example point B lying in this region are shown in Fig. 9, and all of them have simple zeros.

4.3. Semi-chaotic regions

It is interesting that combining the boundaries of chaotic regions for different sets of unperturbed orbits reveals the existence of regions in space (h, γ) which can be called semi-chaotic. In these regions, colored in yellow in Fig. 6, *d*, chaos is possible in the vicinity of only one or two sets of unperturbed orbits, but not near all of them. For instance, at point C (h = 500 km, $\gamma = 3 \cdot 10^{-7}$), one should expect chaos in the vicinity of the inner homoclinic orbits, but not near the inner heteroclinic orbits nor near the outer unperturbed orbits. Indeed, of the three Melnikov functions constructed for these separatrices shown in Fig. 10, only the one corresponding to the inner homoclinic orbits

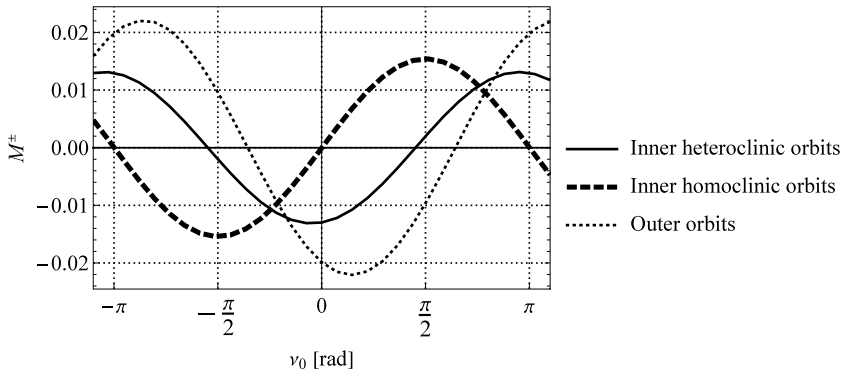

Fig. 9. Melnikov functions corresponding to point B ($h = 550$ km, $\gamma = 10^{-2}$) in Fig. 6, *d*.

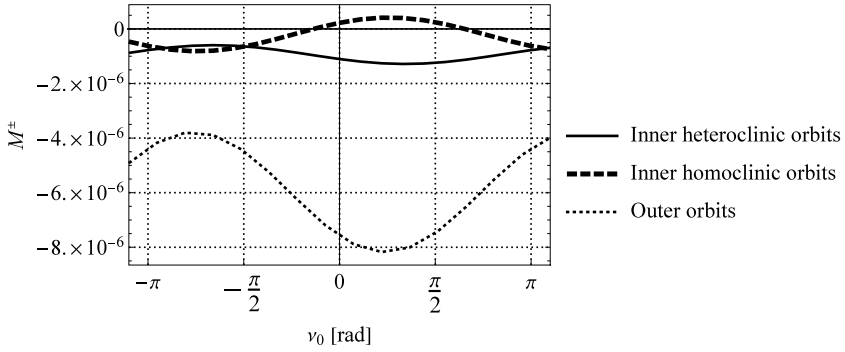

Fig. 10. Melnikov functions corresponding to point C ($h = 500$ km, $\gamma = 3 \cdot 10^{-7}$) in Fig. 6, *d*.

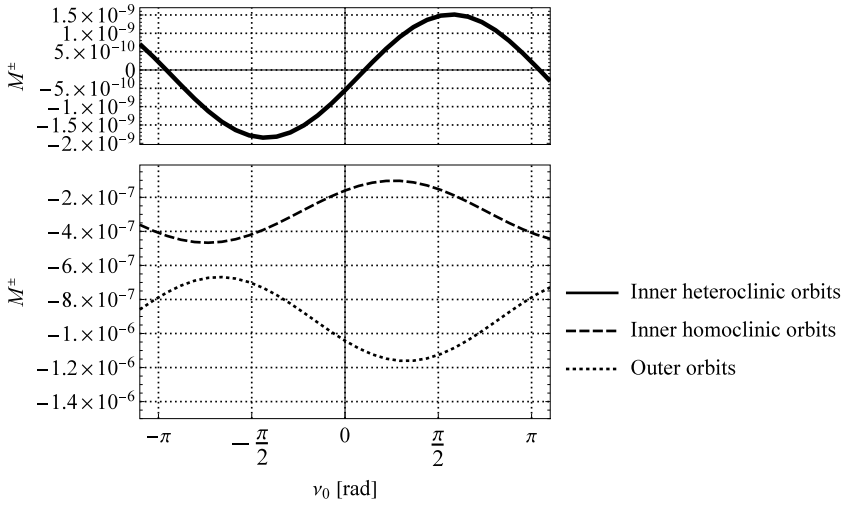

Fig. 11. Melnikov functions corresponding to point D ($h = 596.5$ km, $\gamma = 4 \cdot 10^{-8}$) in Fig. 6, *d*.

has simple zeros. At point D ($h = 596.5$ km, $\gamma = 4 \cdot 10^{-8}$), we observe the opposite situation: chaos is possible in the vicinity of the inner heteroclinic orbits, but not near the inner homoclinic orbits and not near the outer orbits. Fig. 11 demonstrates that only the Melnikov function corresponding to the inner heteroclinic orbits has simple zeros.

5. Poincaré sections

In this section, in order to illustrate the cases of chaotic and regular motion found above using the Melnikov method, the Poincaré surfaces [44] in the two-dimensional $(\theta, \theta' = \omega)$ phase space of the perturbed system are constructed. More specifically, four cases are considered: explicit regular motion, explicit chaotic regime, and two cases corresponding to the semi-chaotic regions in space (h, γ). All the Poincaré surfaces are calculated via the numerical integration of Eq. (10).

5.1. Explicit regular and chaotic regimes

The Poincaré sections for the regular pitch motions corresponding to example point A ($h = 450$ km, $\gamma = 10^{-9}$) in Fig. 6, *d* are shown in Fig. 12. All the phase trajectories shown in Fig. 12, *a* start in the points

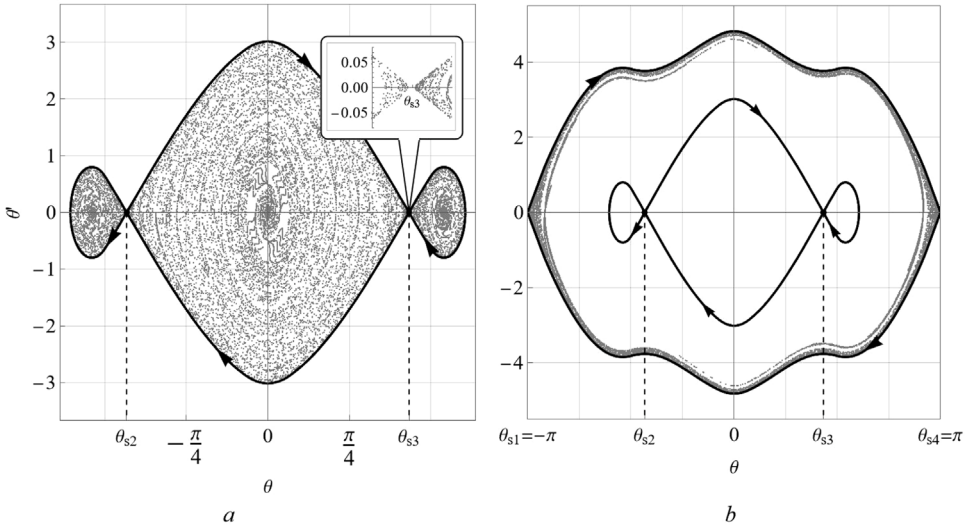

Fig. 12. Poincaré sections for the regular pitch motions corresponding to point A ($h = 450$ km, $\gamma = 10^{-9}$) in Fig. 6, *d*.

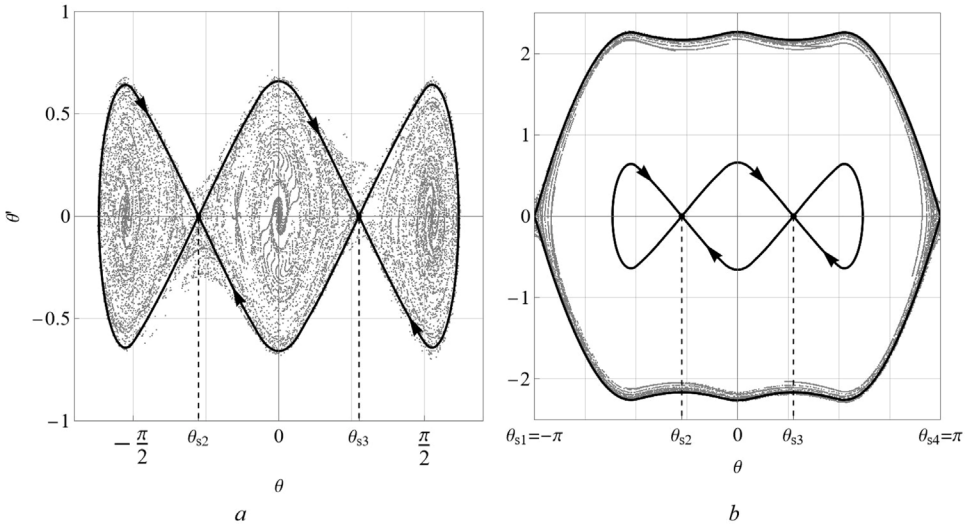

Fig. 13. Poincaré sections for the chaotic pitch motions corresponding to point B ($h = 550$ km, $\gamma = 10^{-2}$) in Fig. 6, *d*.

$$\theta_0 \in (\theta_{c1}; \theta_{c2});\ \theta_0' = 0. \tag{24}$$

It can be clearly seen that there are no intersections between the stable and unstable manifolds in the vicinity of saddle points θ_{s2}, θ_{s3} lying on the inner separatrix. The same is true for the trajectories close to the outer separatrix starting in the points

$$\theta_0 \in (0.9\pi; \pi);\ \theta_0' = 0. \tag{25}$$

and depicted in Fig. 12, *b*, since all the points of the corresponding Poincaré section lie inside the outer separatrix.

The explicit chaotic regime corresponding to the example point B ($h = 550$ km, $\gamma = 10^{-2}$) in Fig. 6, *d* is illustrated by Fig. 13, *a, b*. As in the previous case, the initial points for these Poincaré sections are defined by Eqs. (24) and (25). But due to the fact that with this combination of parameters the aerodynamic damping makes a much smaller contribution to the motion of the system compared to the perturbation from the magnetic torque, the stable and unstable manifolds intersect, and a clearly visible chaotic layer surrounds all four saddle points $\theta_{s1}...\theta_{s4}$. Note that these results are consistent with the earlier results for the pitch motion of a magnetic satellite given in Ref. [13].

5.2. Regular and chaotic regimes for semi-chaotic regions

Fig. 14 shows Poincaré surfaces corresponding to the point C ($h = 500$ km, $\gamma = 3 \cdot 10^{-7}$) in Fig. 6, *d*. All the trajectories shown in Fig. 14, *a* start in the points ($\theta \in [\theta_{s3} + 0.0005, 1.8], \theta'$). These points have the same energy $E = U(\theta_{s3} + 0.0005)$, calculated using Eq. (17), and are located near the inner separatrix in the local potential well bounded by the inner homoclinic orbits (Fig. 4, *a*, bottom). It can be clearly seen that there is a chaotic intersection for the perturbed motion near the inner homoclinic orbits, and the aerodynamic damping in this case does not have a significant impact on the behavior of the system. Fig. 14, *b, c* depicts the trajectories starting in the points ($\theta \in [\theta_{s3} - 0.0005, 1.8], \theta'$). All these points have the same energy $E = U(\theta_{s3} - 0.0005)$ and are located near the inner separatrix in the local potential well bounded, in this case, by the inner heteroclinic orbits. It can be seen that the intersection of the stable and unstable manifolds in the vicinity of the saddle θ_{s3} does not occur, so the aerodynamic damping is sufficient to remove the chaos near the inner heteroclinic orbits.

Fig. 15 illustrates the opposite case, corresponding to the point D ($h = 596.5$ km, $\gamma = 4 \cdot 10^{-8}$) in Fig. 6, *d*. Fig. 15, *a* depicts the trajectories starting in the points ($\theta \in [\theta_{s3} + 0.0002, 2], \theta'$). These points have the same energy $E = U(\theta_{s3} + 0.0002)$ and are located

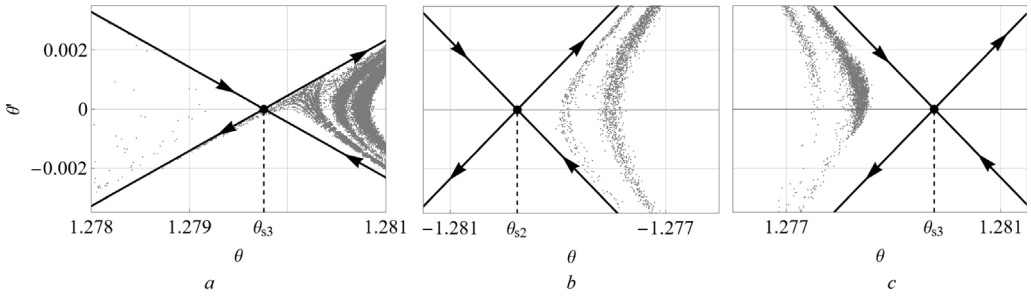

Fig. 14. Poincaré sections for the chaotic (a) and regular (b, c) pitch motions corresponding to point C ($h = 500$ km, $\gamma = 3 \cdot 10^{-7}$) in Fig. 6, *d*.

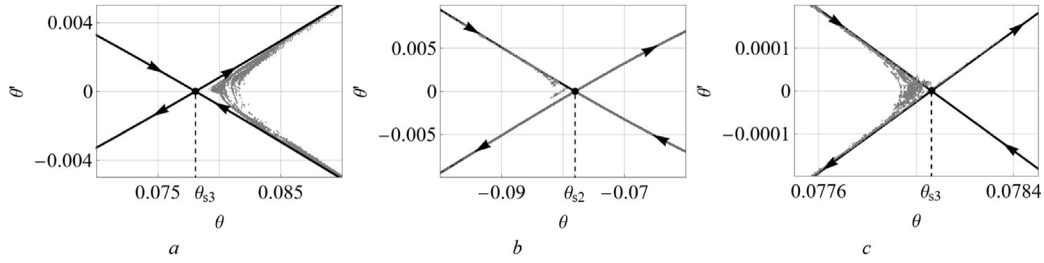

Fig. 15. Poincaré sections for the regular (a) and chaotic (b, c) pitch motions corresponding to point D ($h = 596.5$ km, $\gamma = 4 \cdot 10^{-8}$) in Fig. 6, *d*.

near the inner separatrix in the local potential well bounded by the inner homoclinic orbits. It can be seen that the intersection of the stable and unstable manifolds in the vicinity of the separatrix does not occur. On the contrary, for the trajectories starting in the points $(\theta \in [\theta_{s3} - 0.0002, 2], \theta')$ lying in the central potential well and having the same energy $E = U(\theta_{s3} - 0.0002)$, the points forming the Poincaré sections lie on either side of the inner separatrix (Fig. 15, *b, c*), which indicates the sensitivity to initial conditions and the presence of chaos near saddle points θ_{s2} and θ_{s3}.

Thus, the behavior of the perturbed system predicted by the Melnikov method is confirmed by the Poincaré sections for all three regions in the parameters space (h, γ) found for the example satellite (Fig. 6, *d*): regular, semi-chaotic, and chaotic.

6. Conclusion

In this paper, some features of the pitch motion of aerodynamically stabilized magnetic satellites were studied. On the example of a CubeSat with tail and nose aerodynamic surfaces, it was shown that the unperturbed phase space evolves with orbital altitude both quantitatively and qualitatively, forming different sets of homoclinic and heteroclinic trajectories. With the help of the Melnikov method, the possibility of chaotic attitude motion was demonstrated and the combinations of system parameters corresponding to both regular and chaotic motions were found.

Since the shapes of the aerodynamically stabilized magnetic satellites can differ, it is impossible to give universal recommendations for eliminating chaos in the attitude motion. For each particular satellite, one needs to find the boundaries of chaotic regions, following the proposed procedure, taking into account the orbital altitude and the satellite's own magnetic moment. If the satellite has an aerodynamic instability, its unperturbed phase portrait contains two separatrices that form both heteroclinic and homoclinic orbits, and one needs to bear in mind that there can be situations where chaos is possible in the vicinity of one set of orbits, but not near any other set. In any case, combining the boundaries for each set of the unperturbed orbits gives the resulting boundaries of the regular and chaotic regions. These boundaries can be used for determining the parameters of aerodynamically stabilized magnetic satellites according to the particular objectives of their missions.

The future work will focus on related problems not covered in this paper. In particular, it is interesting to control chaos using magnetorquers or movable aerodynamic surfaces in order to transform irregular attitude motions into periodic ones. Another promising area of research is to investigate the observed effects in a more general case of three-dimensional attitude motion of an aerodynamically stabilized magnetic satellite.

CRediT authorship contribution statement

Vladimir S. Aslanov: Conceptualization, Methodology, Investigation. **Dmitry A. Sizov:** Visualization, Software, Writing – original draft, Writing – review & editing, Validation.

Declaration of competing interest

The authors declare that they have no known competing financial interests or personal relationships that could have appeared to influence the work reported in this paper.

Data availability

No data was used for the research described in the article.

Acknowledgments

This study was supported by the Russian Science Foundation (Project No. 19-19-00085).

Appendix. Coefficients of fourier expansions of aerodynamic torque coefficients of the example satellite

j	$b_{\theta j}$	$a_{\theta j}$	j	$b_{\theta j}$	$a_{\theta j}$
0	–	−13.31	26	0.0003274	0.006417
1	−1.505	−0.07774	27	−0.002994	0.01253
2	0.1051	1.123	28	−0.003383	0.03803
3	−1.586	−0.3846	29	0.006583	0.00544
4	−0.03218	0.2349	30	−0.001573	0.02435

5	0.08895	0.2088	31	−0.0076	−0.001366
6	−0.01313	−0.2462	32	−0.002448	0.0331
7	−0.2027	−0.08099	33	−0.00007569	−0.006126
8	−0.006674	−0.02425	34	8.478e−6	0.005409
9	0.01224	−0.1004	35	−0.009323	−0.007783
10	0.00218	−0.1315	36	−0.001474	0.001224
11	−0.07225	−0.1344	37	−0.0009185	−0.008006
12	−0.001108	−0.02695	38	0.0001594	−0.02015
13	0.01492	−0.07203	39	−0.006959	−0.007289
14	0.002333	−0.09969	40	−0.001004	−0.01294
15	−0.02403	−0.03518	41	0.001048	−0.007801
16	−0.001074	−0.02544	42	0.0003886	−0.01795
17	0.02251	−0.0009436	43	−0.003244	−0.005452
18	0.002022	−0.05379	44	−0.0004595	−0.005608
19	−0.002607	0.01121	45	0.003032	−0.002579
20	−0.0005913	−0.001807	46	0.001229	−0.008233
21	0.02249	0.02323	47	−0.001435	0.001509
22	0.002466	−0.02514	48	−0.00007016	0.001061
23	0.0003728	0.02399	49	0.003464	0.0043
24	−0.0003311	0.01425	50	0.0004146	−0.002175
25	0.01418	0.02036	–	–	–

References

[1] Wytrzyszczak I, Breiter S, Borczyk W. Regular and chaotic motion of high altitude satellites. Adv Space Res 2007;40(1):134–42.

[2] Daquin J, Rosengren AJ, Alessi EM, Deleflie F, Valsecchi GB, Rossi A. The dynamical structure of the MEO region: Long-term stability, chaos, and transport. Celestial Mech Dynam Astronom 2016;124(4):335–66.

[3] Qian Y, Zhang W, Yang X, Yao M. Energy analysis and trajectory design for low-energy escaping orbit in Earth–Moon system. Nonlinear Dynam 2016;85(1):463–78.

[4] Qian Y, Yang X, Jing W, Zhang W. An improved numerical method for constructing halo/lissajous orbits in a full solar system model. Chin J Aeronaut 2018;31(6):1362–74. http://dx.doi.org/10.1016/j.cja.2018.03.006, URL https://www.sciencedirect.com/science/article/pii/S1000936118300980.

[5] Qian Y-J, Liu Z-X, Yang X-D, Hwang I, Zhang W. Novel subharmonic resonance periodic orbits of a solar sail in Earth–Moon system. J Guid Control Dyn 2019;42(11):2532–40.

[6] Li X, Qian Y-J, Yang X-D, Zhang W. Stability and bifurcation analyses for exterior resonant families in Earth-Moon system. Results Phys 2021;31:104961.

[7] Daquin J, Legnaro E, Gkolias I, Efthymiopoulos C. A deep dive into the $2g + h$ resonance: Separatrices, manifolds and phase space structure of navigation satellites. Celestial Mech Dynam Astronom 2022;134(1):1–31.

[8] Zhou Y, Zhang W. Analysis on nonlinear dynamics of two first-order resonances in a three-body system. Eur Phys J Spec Top 2022;1–18.

[9] Iñarrea M, Lanchares V. Chaotic pitch motion of an asymmetric non-rigid spacecraft with viscous drag in circular orbit. Int J Non-Linear Mech 2006;41(1):86–100.

[10] Kemih K, Kemiha A, Ghanes M. Chaotic attitude control of satellite using impulsive control. Chaos Solitons Fractals 2009;42(2):735–44.

[11] Yue B-Z. Study on the chaotic dynamics in attitude maneuver of liquid-filled flexible spacecraft. AIAA J 2011;49(10):2090–9.

[12] Chegini M, Sadati H. Chaos analysis in attitude dynamics of a satellite with two flexible panels. Int J Non-Linear Mech 2018;103:55–67.

[13] Iñarrea M. Chaos and its control in the pitch motion of an asymmetric magnetic spacecraft in polar elliptic orbit. Chaos Solitons Fractals 2009;40(4):1637–52.

[14] Iñarrea M. Chaotic pitch motion of a magnetic spacecraft with viscous drag in an elliptical polar orbit. Int J Bifurcation Chaos 2011;21(07):1959–75. http://dx.doi.org/10.1142/S0218127411029562.

[15] El-Gohary A. Chaos and optimal control of steady-state rotation of a satellite-gyrostat on a circular orbit. Chaos Solitons Fractals 2009;42(5):2842–51.

[16] Kirchgraber U, Manz U, Stoffer D. Rigorous proof of chaotic behaviour in a dumbbell satellite model. J Math Anal Appl 2000;251(2):897–911.

[17] Aslanov V, Yudintsev V. Dynamics and chaos control of gyrostat satellite. Chaos Solitons Fractals 2012;45(9–10):1100–7.

[18] Iñarrea M, Lanchares V, Pascual AI, Elipe A. On the stability of a class of permanent rotations of a heavy asymmetric gyrostat. Regul Chaotic Dyn 2017;22(7):824–39.

[19] Fernández-Martínez M, López MA, Vera J. On the dynamics of planar oscillations for a dumbbell satellite in J_2 problem. Nonlinear Dynam 2016;84(1):143–51.

[20] Doroshin AV. Regimes of regular and chaotic motion of gyrostats in the central gravity field. Commun Nonlinear Sci Numer Simul 2019;69:416–31.

[21] Aslanov VS. Chaotic attitude dynamics of a LEO satellite with flexible panels. Acta Astronaut 2021;180:538–44.

[22] Aslanov VS, Sizov DA. Chaos in flexible CubeSat attitude motion due to aerodynamic instability. Acta Astronaut 2021;189(May):310–20. http://dx.doi.org/10.1016/j.actaastro.2021.08.055.

[23] Lanchares V, Iñarrea M, Pascual AI, Elipe A. Stability conditions for permanent rotations of a heavy gyrostat with two constant rotors. Mathematics 2022;10(11). http://dx.doi.org/10.3390/math10111882, URL https://www.mdpi.com/2227-7390/10/11/1882.

[24] DeBra DB. The effect of aerodynamic forces on satellite attitude. J Astronaut Sci 1959;6(3):40–5.

[25] Beletskii VV. Motion of an artificial satellite about its center of mass. 1966, NASA TT F-429.

[26] Sarychev V. Aerodynamic stabilization system of the satellite. In: Proc. of the international conference on attitude changes and stabilization of satellites. 1968, p. 177–83.

[27] Frik MA. Attitude stability of satellites subjected to gravity gradient and aerodynamic torques. AIAA J 1970;8(10):1780–5. http://dx.doi.org/10.2514/6.1969-832.

[28] QARMAN - QubeSat for aerothermodynamic research and measurements on ablation. 2022, URL https://www.vki.ac.be/index.php/qarman-home. [Accessed 21 June 2022].

[29] Crisp NH, Roberts PC, Livadiotti S, Rojas AM, Oiko V, Edmondson S, et al. In-orbit aerodynamic coefficient measurements using SOAR (Satellite for Orbital Aerodynamics Research). Acta Astronaut 2021;180:85–99.

[30] Psiaki ML. Nanosatellite attitude stabilization using passive aerodynamics and active magnetic torquing. J Guid Control Dyn 2004;27(3):347–55.

[31] Rawashdeh SA, Lumpp JE. Aerodynamic stability for CubeSats at ISS orbit. J Small Satell 2013;2(1):85–104.

[32] Guglielmo D, Omar S, Bevilacqua R, Fineberg L, Treptow J, Poffenberger B, et al. Drag deorbit device: A new standard reentry actuator for CubeSats. J Spacecr Rockets 2019;56(1):129–45. http://dx.doi.org/10.2514/1.A34218.

[33] Aslanov V, Sizov D. 3U CubeSat aerodynamic design aimed to increase attitude stability and orbital lifetime. In: 71st international astronautical congress. IAC, 2020.

[34] Graham J, Creed L, Jenkins C, Wilson AR, Vasile M. The design of a fragmentation experiment for a CubeSat during atmospheric re-entry. In: 72nd international astronautical congress. 2021.

[35] Gallais P. Atmospheric re-entry vehicle mechanics. Springer Science & Business Media; 2007.

[36] Shrivastava S, Modi V. Satellite attitude dynamics and control in the presence of environmental torques-A brief survey. J Guid Control Dyn 1983;6(6):461–71.

[37] Hughes PC. Spacecraft attitude dynamics. Courier Corporation; 2004.

[38] Schaaf S, Chambre P. Flow of rarefied gases, high speed aerodynamics and jet propulsion. In: Fundamentals of gas dynamics, vol. 3. Princeton University Press NY; 1958.

[39] Wilmoth RG, Mitcheltree RA, Moss JN. Low-density aerodynamics of the stardust sample return capsule. J Spacecr Rockets 1999;36(3):436–41. http://dx.doi.org/10.2514/2.3464.

[40] International standard ISO 14222:2013. Space environment (natural and artificial) — Earth upper atmosphere. 2013, URL https://www.iso.org/standard/54507.html. [Accessed 21 April 2021].

[41] Melnikov VK. On the stability of a center for time-periodic perturbations. Trans Moscow Math Soc 1963;12:3–52.

[42] Guckenheimer J, Holmes P. Nonlinear oscillations, dynamical systems, and bifurcations of vector fields. Springer Science & Business Media; 2013.

[43] Zheng Y, Zhang W, Liu T, Zhang Y. Resonant responses and double-parameter multi-pulse chaotic vibrations of graphene platelets reinforced functionally graded rotating composite blade. Chaos Solitons Fractals 2022;156:111855.

[44] Wiggins S. Introduction to applied nonlinear dynamical systems and chaos, vol. 2. Springer Science & Business Media; 2003.